Journal of Aerosol Science 41 (2010) 587–601

Contents lists available at ScienceDirect

Journal of Aerosol Science

journal homepage: www.elsevier.com/locate/jaerosci

Effects of airway obstruction induced by asthma attack on particle deposition

Kiao Inthavong [a], Jiyuan Tu [a,*], Yong Ye [a], Songlin Ding [a], Aleks Subic [a], Frank Thien [b]

[a] School of Aerospace, Mechanical and Manufacturing Engineering, RMIT University, PO Box 71, Bundoora Vic 3083, Australia
[b] Box Hill Hospital, Eastern Health and Monash University, Australia

ARTICLE INFO

Article history:
Received 6 January 2009
Received in revised form
2 March 2010
Accepted 6 March 2010

Keywords:
Asthmatic airways
Airflow patterns
Particle deposition
Modeling

ABSTRACT

Two computational models of the airway tree up to six generations deep were reconstructed from computed tomography scans from a single patient. The first scan was taken a day after an acute asthma episode while the second scan was taken 30 days later when the patient had recovered. The reconstructed models were used to investigate the effects of acute asthma on realistic airway geometry, the airflow patterns, the pressure drop, and the implications it has on targeted drug delivery. Comparisons in the geometry found that in general the average increase in diameter was larger in the right airway the airway is larger in diameter than the left side. The average airway branch difference from the Asthma Model to the Recovered Model was found to be 10.4% in the right airway and 4.8% in the left airway; however the airway dilation during the recovery stage was not consistent through the entire branch airway. Instead there were local branches that exhibited a very high local dilation recovery ($\approx 30\%$ recovery). This inconsistent dilation recovery makes it difficult to predict where and how much each branch will recover from an asthma episode. In terms of targeted drug delivery studies in the lung airways, the deposition patterns will be under-predicted for airway models that are reconstructed from a healthy or non-asthma affected lung airway. The discrepancy may reach as high as 13% between the two models for particles $\geq 10\,\mu m$ under a turbulent flow. For particles $< 10\,\mu m$, the discrepancy reduces to 1% as the particle size reduces to $1\,\mu m$ under a turbulent flow. This means that drug delivery studies in the lung airway should consider the effects of airway narrowing and that if a recovered or a healthy airway is used, then the deposition fraction and efficiencies are expected to be under-predicted.

1. Introduction

Acute asthma manifests itself most commonly as wheezing, coughing, chest tightness, shortness of breath, and sputum production. Causes of asthma have been attributed to many factors including the inhalation of allergens and toxic particles found in the surrounding environment. The treatment of asthma is often reliant on aerosolised beta-adrenergics, parasympatholytics, and corticosteroids which are delivered into the airways through nebulisers or metered-dose inhalers. However the targeted drug delivery is not efficient. Currently marketed inhalation therapies can only deliver an effective inhalation of 10–20% of a drug load into the lung (Clark, 1995) while Roland, Bhalla, and Earis (2004) reviewed that the

* Corresponding author. Tel.: +61 3 9925 6191; fax: +61 3 9925 6108.
E-mail address: jiyuan.tu@rmit.edu.au (J. Tu).

0021-8502/$ - see front matter Crown Copyright © 2010 Published by Elsevier Ltd. All rights reserved.
doi:10.1016/j.jaerosci.2010.03.001

extra drug load (80–90%, the rest of the drug) in certain drugs may in fact cause side effects to the patient. Since particles are transported by the inhaled air, studies of the airflow mechanisms and patterns within the airway can provide data that is pertinent to the prediction of gas-particle flows and regional tissue exposure to contaminated air and other clinical respiratory research.

The earliest studies of airflow in the lung airways was the experimental work by Schroter and Sudlow (1969). A few velocity profiles and flow patterns were presented for a double-bifurcation model. In other experimental studies the central airway up to the third generation of the bifurcation was used (Chang & El Masry, 1982; Isabey & Chang, 1981). It was concluded that flow patterns were most likely dependent on the airway geometry. In the above studies, the respiratory flow was treated as a steady or quasi-steady condition based on the Womersley parameter for normal breathing. Airflow patterns change as a result of an acute asthma episode where the combination of bronchospasm, mucus plugging, and mucosal edema build up leads to increased airway resistance as the diameters of the airways are reduced. Experimental studies with human subjects have shown that patients with asthma produce different particle deposition patterns (Chalupa, Morrow, Oberdorster, Utell, & Frampton, 2004; Martonen, Fleming, Schroeter, Conway, & Hwang, 2003; Sbirlea-Apiou et al., 2004). Since the nature of *in vivo* studies can be invasive many alternate studies make use of replica and computational models. However most of these studies have considered airflow patterns affected by tumours, airway constrictions and airway blockage associated with chronic obstructive pulmonary disease (COPD) in local subregions of the lung airways. For example, Kim and Kang (1997a) studied local deposition efficiencies and deposition patterns of ultrafine particles in a sequential bifurcation tube model in normal airways and with obstructive airway disease; Musante and Martonen (2001) investigated the effects of both sidewall and carinal tumours on a single symmetric bifurcation under sedentary conditions; Zhang, Kleinstreuer, Kim, and Hickey (2002) studied the airflow and deposition of micron-size particles in a triple lung bifurcation affected by sidewall tumours in generations G3–G6; Yang, Liu, and Luo (2006) demonstrated the importance of the boundary conditions within a locally obstructed airway (generations G5–G8); and Farkas and Balásházy (2007) simulated the effect of local obstructions and blockage on the deposition of aerosols in the lung airway subregion of G3–G5. The work by Longest, Vinchurkara, and Martonen (2006) however, included double bifurcation models of upper (G3–G5) and central (G7–G9) airways for a four-year-old child where the effects of asthma was modelled as a 30% constriction of the airway branches. Additional studies in obstructed airways (Kim, Brown, Lewars, & Sackner, 1983; Kim, Eldridge, Garcia, & Wanner, 1989; Kim, 1989; Kim & Kang, 1997b), showed that greater deposition occurred in the obstructed lung compared with a normal lung.

In the above studies, lung subregions of interest were reconstructed from Weibel's (1963) model and airway constrictions were modelled by decreasing the airway diameters. This paper extends these ideas by reconstructing two computational models of the tracheobronchial airway tree down to the sixth generation from computed tomography (CT) scans of a single patient. The first scan was taken a day after an acute asthma episode while the second scan was taken 30 days later when the patient had recovered. Comparisons between the two models are made in terms of (i) the geometric changes in the airway and (ii) the significance of the airway geometry change on the airflow patterns and particle deposition. Since the intention of drug delivery studies is to better understand and deliver drug particles more efficiently, the results of this comparative model study can help determine whether using a single recovered or non-asthmatic airway model is sufficient for drug delivery studies or whether the model indeed needs to be reconstructed from an asthma-affected patient. In addition some of the data can help to reveal what scales of magnitudes exist in the airway recovery 30 days after the onset of asthma.

While most deposition studies have used Weibel's (1963) model and considered the bifurcation airways as symmetric, the use of realistic models then leads to a lack of exact matching of comparative/compatibility studies as the data does not necessarily exist in the literature unlike the data for Weibel's model. The authors have adopted the method by Luo and Liu (2009) which compared their CFD model against (de Rochefort et al., 2007)'s experimental data, the method by van Ertbruggen, Hirsch, and Paiva (2005) which compared their CFD model against (Calay, Kurujareon, & Holdo, 2002)'s numerical predictions, and the method by Choi, Tu, Li, and Thien (2007) which compared with Schlesinger, Gurman, and Lippmann (1982) and Kim and Fisher (1999)'s data. This paper follows the same approach in conducting comparisons of CFD with the available data. The results in this paper are not intended to be a generalization but rather to contribute towards establishing data for future comparative benchmarks such as the work by Calay et al. (2002), and to present the modelling requirements, techniques, and different analysis methods. For generalised findings, the use of a general model such as the standard Weibel model is a common method for deposition studies (Hofmann, Golser, & Balashazy, 2003; Longest & Vinchurkar, 2009). The use of a large number of models has only been performed by De Backer et al. (2008) which used 14 models to produce a general trend to detect changes in airway resistance in asthmatics.

2. Method

2.1. CT scans and image segmentation

The first two models were developed from CT scans from a 66-year-old non-smoking, asthmatic male (height 171 cm and weight 58 kg) using a helical 64 slice multidetector row CT scanner (General Electric) the day after hospital admission with an acute exacerbation of asthma. At the time, his lung function by spirometry (Spirocard, QRS Diagnostic, Plymouth,

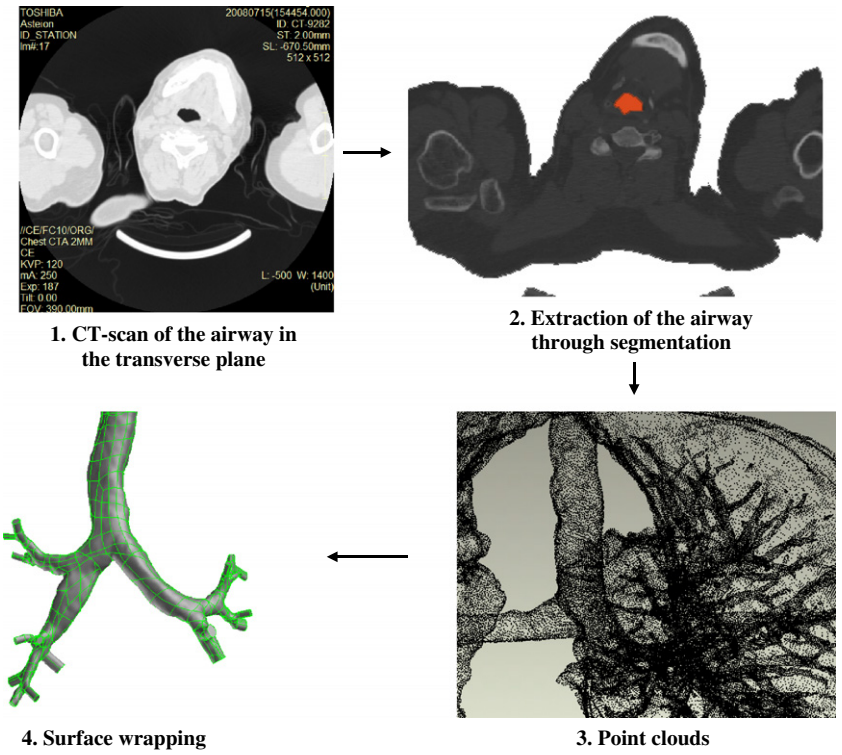

Fig. 1. Steps in the reconstruction of the airway from CT-scans to a 3D surface model.

Minnesota, USA) showed severe airflow obstruction with a forced expiratory volume in 1 s (FEV_1) of 1.02 L (41% predicted). Data was acquired with 1 mm collimation, a 40 cm field of view (FOV), 120 kV peak and 200 mA. At baseline, 2 cm axial length of lung caudal to the inferior pulmonary ligament was scanned during a single full inhalation total lung capacity breath-hold, which yielded 254 contiguous images (slices) of 1 mm thickness with voxel size of $0.625 \times 0.625 \times 1$ mm. An identical protocol was used to acquire images following recovery 30 days later, when his FEV1 was measured at 2.27 L (91% predicted). The two computationally reconstructed models were then identified as the Asthma Model (acute asthma model) and the Recovered Model. The process in creating the CFD model from CT-scans is not unique and different methods can be applied. A generic process is shown in Fig. 1. CT scans produce contiguous slices of the airway and stores the images as Digital Imaging and Communications in Medicine (DICOM) standard, which is commonly used for the transfer and storage of medical images. The segmentation step involves extraction of the region of interest, i.e. the airway region. The segmentation provides data points in space. These points are known as 'cloud points' that represent actual points that lie on the surface of the object. An actual surface that wraps around the object has to be created by effectively joining up the cloud points. Finally the surfaced model can then be imported into any CFD Pre-processor for meshing. Using the meshing software Gambit 2.2 (ANSYS Inc.), the face, volume, mesh and extension tubes at outlets were created and a mesh file was produced, which was then read into Fluent 6.3 (ANSYS Inc.).

2.2. *Fluid flow modelling*

For this study the method adopted from Balashazy and Hofmann (1993), Longest et al. (2006), Zhang and Kleinstreuer (2001), and Zhang et al. (2001) where a laminar and a turbulent parabolic inlet profile from an extended trachea is used. In a recent study by Li, Kleinstreuer, and Zhang (2007b), it was found that the type of velocity inlet condition and existence of cartilaginous rings influences the air flow field; however, their impact is less important in comparison with the variations in the upper airway geometry, e.g., branch curvature. Two flow rates 10 L/min, Re=700 and 30 L/min, Re=2310 were used which can be representative of low inhalation and a rapid, high-intense inhalation, respectively. A laminar flow model was used for the Re=700 case while the low Reynolds number (LRN) k–ω model was used for the Re=2310 case. At a flow rate of Re=700 the flow is dominantly laminar and transitional behaviour may occur downstream as secondary flow phenomena are induced by the bifurcations. The effects of the transition from laminar to turbulent flow are best captured with sophisticated turbulence models such as Large Eddy Simulations or the Direct Numerical Solution approach. The LRN turbulence models can also resolve the transition behaviour but requires near wall damping modifications that reduce the length scales of the turbulent fluctuating velocities and increase the dissipation rate. In addition a fine mesh in the near wall region with a $y^+=1$ is needed. In any turbulent model, the behaviour of the turbulent boundary layer is captured from

the wall to the outer free stream which is considered a fully turbulent flow. This assumption may not always be appropriate for laminar dominant flows since the solution will over predict the diffusion due to the inherent turbulence production from the eddy viscosity.

An exact model of the airway would include of the mouth opening, oral cavity, larynx and therefore the laryngeal jet, however one limitation of this study is the unavailable data for the larynx due to the CT scan acquisition. CT-scans produce radiation to the patient and therefore acquired scans are limited by an exposure time. Slices can be taken at a greater contiguous distance which increases the scanned region; however this increases the interpolation needed between each slice and may compromise the exact replication of the airway replication. The absence of the laryngeal jet is expected to produce an under-prediction of the deposition efficiency in the first bifurcation at the carina. However deeper into the lung airways the effects of the laryngeal jet begins to diminish.

A steady flow was applied based on a variety of criteria (Isabey & Chang, 1981; Slutsky, Berdine, & Drazen, 1981; Sullivan & Chang, 1991) such as the Womersley parameter, $\alpha = D/2(\omega/v_g)^{0.5}$; a variant of the Womersley parameter, $\alpha^* = 1/2(\omega D/0.0075u_{ave})^{0.5} < 1$ (Pedley, Schroter, & Sudlow, 1977); and the Strouhal number, $S = \omega D/u_{ave}$ where u_{ave} is the mean velocity, ω is the angular frequency of oscillation ($=2\pi f$), D is the diameter of the tube and v_g is the viscosity.

The outlets at the sixth generation branches were artificially extended downstream given by, $L_{extension} = 0.05\,\mathrm{Re}\,D$ to obtain fully developed profiles and hence avoid any reverse flow that may be caused, due to an abrupt end to the flow field. Each model underwent mesh refinement by cell adaption techniques that included refining large volume cells, cells that displayed high velocity gradients, and near wall refinements. Velocity profiles were compared between each subsequent model until the profiles remained the same and hence became independent of the grid size. The final model had a mesh size of 1.5 million cells and is shown in Fig. 2. A schematic diagram which shows the details the branches of the model and the definition of the dorsal angle measurement used in Table 1 is shown in Fig. 3. The airway tree was constructed from unstructured tetrahedral cells and the commercial CFD code, FLUENT was used to predict the continuum gas phase flow under steady-state, isothermal, and incompressible conditions through solutions of the conservation equations of mass and momentum. These equations in Cartesian tensor notation are:

$$\frac{\partial}{\partial x_i}(\rho u_i) = 0 \tag{1}$$

$$\rho u_k \frac{\partial u_i}{\partial x_k} = -\frac{\partial p}{\partial x_k} + \frac{\partial}{\partial x_k}\left(\mu\left(\frac{\partial u_i}{\partial x_k} + \frac{\partial u_k}{\partial x_i} - \frac{2}{3}\delta_{ij}\frac{\partial u_i}{\partial x_k}\right)\right) + \frac{\partial}{\partial x_k}(-\rho\overline{u_i' u_k'}) \tag{2}$$

The transport equations for the turbulent kinetic energy, k and the dissipation rate, ω are:

$$\rho u_i \frac{\partial k}{\partial x_k} = \frac{\partial}{\partial x_k}\left(\mu + \frac{\mu_t}{\sigma_k}\right)\frac{\partial k}{\partial x_k} + G_k - Y_k + S_k \tag{3}$$

$$\rho u_i \frac{\partial \omega}{\partial x_k} = \frac{\partial}{\partial x_k}\left(\mu + \frac{\mu_t}{\sigma_\omega}\right)\frac{\partial \omega}{\partial x_k} + G_\omega - Y_\omega + S_\omega \tag{4}$$

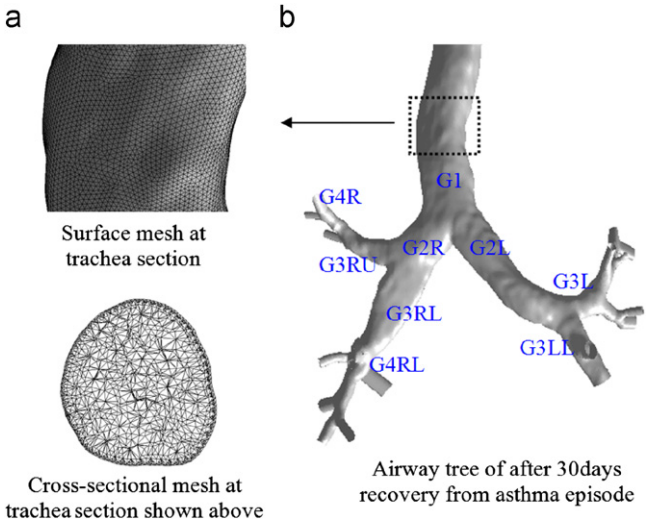

Fig. 2. Computational model of the upper tracheobronchial airway tree with branch identification. The first two characters define the branch generation. The third character represents the right or left airway. The fourth character may be U, M or L representing upper, middle and lower, respectively. The definition of the dorsal branching angle for the G3L branch is also shown.

Table 1
Average diameter of the tracheobronchial tree model (dimensions in millimeters).

Measurement in millimetres **Diameter**	**TRACH**	**G1**	**G2R**	**G2L**	**G3R**	**G3L**
Asthma affected model	18.0	15.4	11.2	8.8	A: 5.0 B: 8.2	A: 6.2 B: 5.8
Recovered model	18.5	15.8	11.6	9.2	A: 5.8 B: 8.7	A: 6.1 B: 6.6
Other[a]	19	9–16	7–11		5–7	
Branching angles	**G1-G2**	**G2-G3R**	**G2-G3L**	**G3L-Dorsal Angle**[b]		
Asthma affected model	79°	89°	96°	24°		
Recovered model	81°	90°	91°	31°		

[a] Other measurements were extracted from Weibel (1963) for diameter and length and Sauret et al. (2002) for branching angle. Weibel (1963) measured a cadaver's airway and reported in a range value for each generation. Sauret et al. (2002)'s measured a healthy male volunteer's airway using CT images and reported the range value for all generations.
[b] See Figs. 2 and 5 for airway schematic.

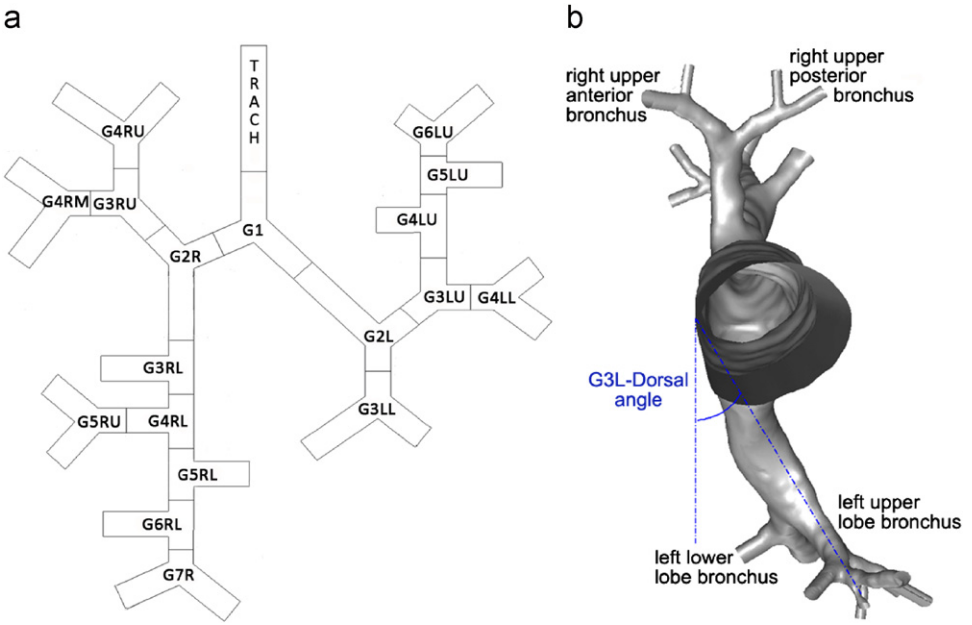

Fig. 3. (a) Schematic diagram corresponding to the geometry shown in Fig. 2 with branch identification inside each branch and (b) Dorsal angle definition used in the measurements found in Table 1. Some bronchi are also labelled.

The third-order accurate QUICK scheme was used to approximate the momentum equation while the pressure–velocity coupling was resolved through the SIMPLE method. The convergence criteria for the air flow properties (resolved velocities and pressure) were set at 10^{-5}.

2.3. *Particle flow modelling*

Particles were tracked through a force balance equation

$$\frac{du_i^p}{dt} = F_D(u_i^g - u_i^p) + \frac{g(\rho_p - \rho_g)}{\rho_p} + S_i \tag{5}$$

F_D is the drag force per unit particle mass

$$F_D = \frac{18\rho_g}{\rho_p d_p^2}\frac{C_D \mathrm{Re}}{24} \tag{6}$$

Re is the particle Reynolds number, which is defined as

$$\mathrm{Re} \equiv \frac{\rho_g d_p |u^p - u^g|}{\mu} \tag{7}$$

where u^g, u^p, μ, ρ_g, ρ_p and d_p are gas (air) velocity, particle velocity, molecular viscosity of the fluid, fluid density, particle density and particle diameter, respectively. The drag coefficient, C_D, is evaluated from an experimental-fitted expression given by Morsi and Alexander (1972). For 1 μm particles that exhibit slip between the particle and fluid, a Cunningham Correction factor is applied.

$$C_c = 1 + \frac{2\lambda}{d_p}(1.257 + 0.4e^{-(1.1 d_p/2\lambda)}) \tag{8}$$

The gas velocity u_i^g found in the slip velocity $(u_i^g - u_i^p)$ of Eq. (7) is defined from the cell centre and a particle within any part of that cell takes u_i^g from the cell centre. For cells adjacent to the wall boundaries, the velocity profile should approach zero at the wall rather than be uniform throughout the cell. Therefore a near wall interpolation (NWI) scheme defined by,

$$U_i^g = \frac{U_1/L_1 + U_2/L_2 + U_3/L_3 + U_4/L_4}{1/L_1 + 1/L_2 + 1/L_3 + 1/L_4} \tag{9}$$

is applied to all wall adjacent cells and is shown in Fig. 4. The NWI takes into account the influence of the zero velocity at the wall boundary as well as the convective fluxes of the surrounding cells.

The force balance equation was integrated through the fifth order Runge–Kutta scheme derived by Cash and Karp (1990) which uses an embedded error control mechanism to accelerate the solution. For the turbulent dispersion of particles, a Monte Carlo type stochastic process called the Eddy Interaction Model or the Discrete Random Walk model in Fluent is applied. The fluid velocity u_i^g in Eq. (5) becomes $u_i^g + u_i'(t)$ which represents a fluid eddy where

$$u_i' = \zeta\sqrt{\overline{u_i'^2}} \tag{10}$$

ζ is a normally distributed random number and the remaining right-hand side is the local root mean square (RMS) velocity fluctuation obtained from the turbulent kinetic energy, k.

$$\sqrt{\overline{u_i'^2}} = \sqrt{2k_g/3} \tag{11}$$

The interaction time between the particles and eddies is smaller of the eddy lifetime τ_e and the particle residence time within the eddy. The characteristic lifetime of the eddy is defined as:

$$\tau_e = -T_L \log(r) \tag{12}$$

where T_L is the fluid Lagrangian integral time approximated as $T_L = 0.3(k/\varepsilon)$. The stochastic dispersion is made consistent with the eddy lifetime which needs to randomised (Kallio & Reeks, 1989) through the probability variable, r which is a uniform random number between 0 and 1. The particle–eddy interaction ends once the particle has left the eddy or the eddy lifetime is over. The particle then encounters a new eddy at its current location, and the process repeats until a particle is deposited onto a wall or escapes through the branch outlets. Some drawbacks of the model include the unrealistic dispersion caused in flows with large relative velocity fields, and the unphysical discontinuity of the new fluctuating velocity as the particle enters a new fluid eddy. Despite this, the model has been widely used and has shown to produce realistic deposition rates when the isotropic turbulent assumption problem with RANS turbulence model is damped in the near wall region (Graham & James, 1996; Wang & James, 1999; Zhang, Finlay, & Matida, 2004). The damping

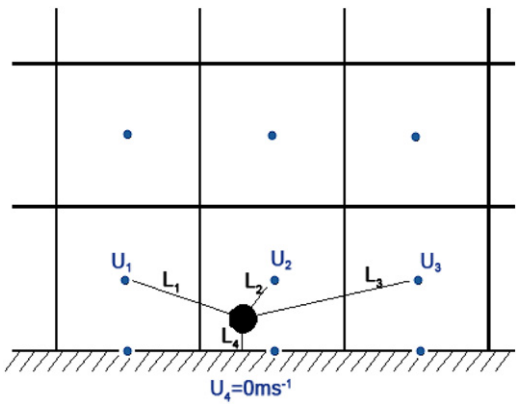

Fig. 4. Near wall interpolation scheme applied to all wall adjacent cells.

function given in Matida, Finlay, Lange, and Grgic (2004) is used here and is given below:

$$u'_g = v'_g = w'_g = [1-\exp(-0.02y^+)] \cdot (2k/3)^{1/2} \quad (13)$$

The dependency of the deposition results on the number of particles was tested. The number of particles for 5 μm was increased from 20,000 up to 200,000. The final particle number which became independent of the number of particles was found to be approximately 120,000. The total deposition efficiency is the total number of particles depositing in the tracheobronchial airway up to the sixth generation divided by the number of particles introduced. The particle fraction is calculated as the number of particles depositing locally divided by the number of particles introduced, i.e. $\eta_{\text{fraction}} = N_{local}/N_{totalin}$.

One way coupling is assumed between the air and particle flow fields and the interaction between particles is also neglected because the particle flow is dilute (i.e. the volume fraction of the particles is $< 10\%$). S_i is additional forces that include the Saffman lift force, pressure force, buoyancy force, virtual mass effect and Basset force. Solid aerosols such as drug particles or toxic fibres are generally in the micron size range and typically far denser than air, causing terms that depend on the density ratio, such as those in S_i to be negligibly small.

3. Results

3.1. Airflow distribution validation

Normalised velocity profiles in the trachea and main bronchi were compared with two sets of experimental data. The first comparison is made against the experimental data of (de Rochefort et al., 2007) which reconstructed a physical cast model from CT lung scans of a 59-year-old male (Fig. 5). The CFD model was obtained from CT scans of a 66-year-old non-smoking, asthmatic male. The second velocity profile comparison was made against a 3:1 scaled up acrylic plastic model of the human central airways (Menon, Weber, & Chang, 1984). The velocity profiles generally have good agreement with experimental results in terms of the main flow features. Discrepancies are found at some of the cross-sections which may be due to a combination of airway geometry differences, and the experimental model having a surface roughness which is not modelled in the CFD.

The velocity contour and profile at S1 shows the effects of the bifurcation where high velocity remains near the inner region of the bifurcation (Fig. 6). Further downstream the profile at S2 shows the flow beginning to bifurcate which explains the bi-modal peaks in the velocity profile. In Fig. 7, S3 shows a slight parabolic shape as expected from a fully developed flow. The flow splits at the first bifurcation and the profiles are skewed toward the inner regions of the

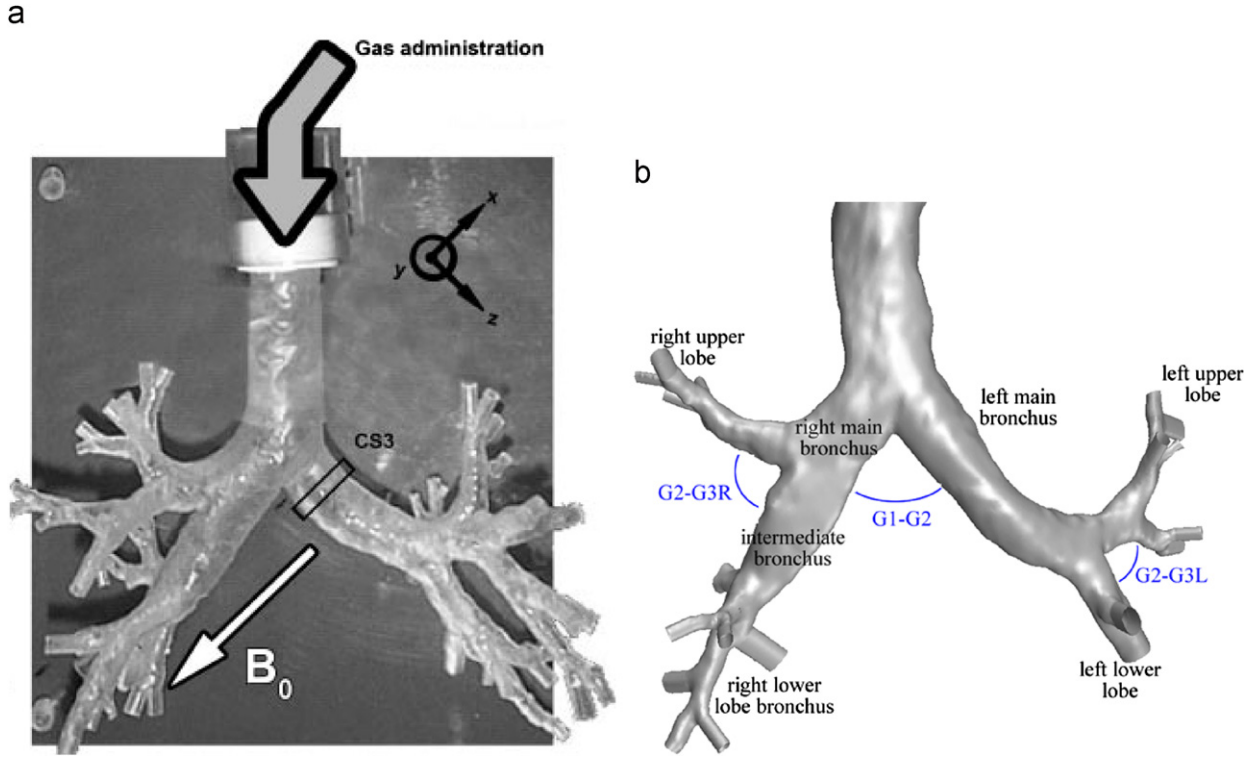

Fig. 5. Model comparisons between the (a) physically reconstructed model taken from the work of de Rochefort et al. (2007) and (b) computationally reconstructed model used in the current CFD simulations.

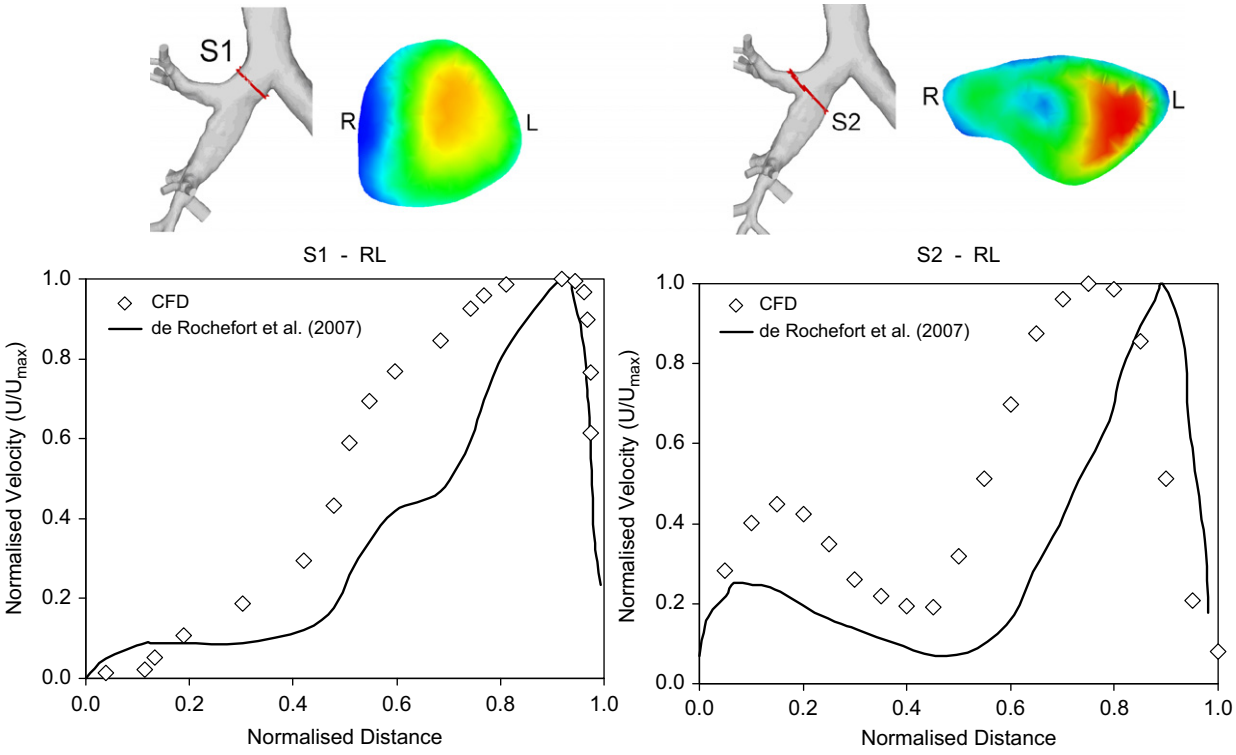

Fig. 6. Normalised velocity profiles comparisons with the work of de Rochefort et al. (2007).

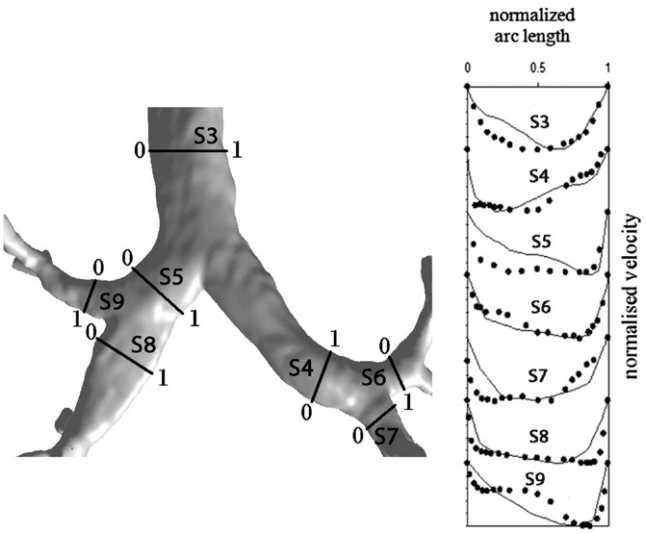

Fig. 7. Normalised velocity profiles (lines) taken at seven different sections, labelled by the prefix S compared against the experimental data (●) of Menon et al. (1984) for the Recovered Model.

bifurcation as shown at S5, which is located in between S1 and S2. The skewed profile prevails in the left main bronchus and is present at S4. The second bifurcation in the left lung airway produces a slightly more skewed profile in the daughter branch with the S6 profile. The S7 profile is less skewed. This is caused by the local bifurcation which forces the upstream bulk flow that was biased towards the inferior side of the branch to merge closer to the middle of the parent branch because of the counter orientation of the S6 daughter branch. The velocity field at S9 continues the upstream profile where the bulk flow remains close to the inner bifurcation wall. The S8 profile begins to recover towards a more parabolic profile as the local bifurcation redistributes the flow to the daughter branches. During this process the upstream bulk flow that is skewed towards the left side of the branch redistributes towards the centre as it begins to split into two flow paths.

3.2. Particle deposition validation

The deposition fraction in the first bifurcation is shown and compared with some existing data in literature (Balásházy, Hofmann, & Martonen, 1990; Cai & Yu, 1988; Kim & Fisher, 1999; Li, Kleinstreuer, & Zhang, 2007a). The deposition fraction combines the particle deposition from both laminar and turbulent simulations and is normalised by the local Stokes number (local average diameter and local average flow velocity). In the first bifurcation the average hydraulic diameters and velocities are 0.0178 m and 0.428 m/s, 0.0184 m and 0.415 m/s, for the recovered model and asthma-affected models, respectively. The results without any modifications to the standard Fluent tracking models shows an over prediction for all cases (Fig. 8a) due to the overprediction of the normal fluctuating velocity, (u'), which is significant for deposition of inertial particles. This overprediction caused by the DRW turbulent dispersion model is most significant for smaller Stokes number particles which produced very high deposition. The damping function in Eq. (11) reduces the normal fluctuation component which provides an improved rate of deposition in Fig. 8b. In addition the application of the NWI given in Eq. (9) reduces the fluid velocity magnitude to zero within the wall adjacent cells as the distance from the wall approaches zero. This provides a better representation of the near wall boundary layer which varies in the perpendicular direction to the wall. The two additional modifications reduce the deposition fraction for all Stokes number and are more aligned with the experimental results.

While it is intuitive to expect that for two particles exhibiting the Stokes number, the deposition efficiency will be the same, it should not necessarily be expected when the airflow is not uniform. The Stokes number normalises the particle inertial properties through the ratio of the particle response time $\tau_{particle} = \rho_p d_p^2/18\mu_g$ to the fluid characteristic time $\tau_{air} = D/U$. This is most appropriate in simple geometries such as pipe flows where the flow is more uniform and the characteristic dimension (usually the hydraulic diameter) of the fluid flow is easily characterised by the diameter of the pipe. Therefore while a local Stokes number is more specifically representative of its nearby regions, it is still representative of an averaged value for the characteristic dimension, and average velocity chosen. Take for example the cross-section S2 in Fig. 6. The local Stokes number based on this cross-section does not reflect the micro flow structures which show a non-uniform profile where high velocity is concentrated at the inner walls of the bifurcations. Therefore enhanced deposition will occur at the inner walls. The micro flow characteristic effect caused by the airway geometry is further pronounced as the flow rate increases and therefore the deposition efficiency does not necessarily have to be the same for the same particle Stokes number (see results of Zhou and Cheng, 2005).

3.3. Airway geometry differences

The reconstructed model of the tracheobronchial tree exhibits an asymmetric dichotomous branching pattern. The beginning of the airway begins with the trachea, which is a hollow cylinder in the shape of a horseshoe due to the C-shaped supporting cartilage found anteriorly and laterally. Completing the tracheal cylinder on the posterior side is a flat band of muscle and connective tissue called the posterior tracheal membrane. Further downstream, the cartilage support becomes progressively smaller and less complete. Average branch diameters and bifurcation angles between daughter branches are given in Table 1.

The equivalent hydraulic diameter, D_h defined by $D_h = 4A_c/P$, where A_c is the cross-sectional area and P is the perimeter, was calculated for the entrance and bifurcating ends of each generation branch. The diameters given in Table 1 for each generation branch is taken as the average diameter from different slices through the branch and a comparison is made between the acute asthma model, the recovered model and results from other airway models (Sauret, Halson, Brown,

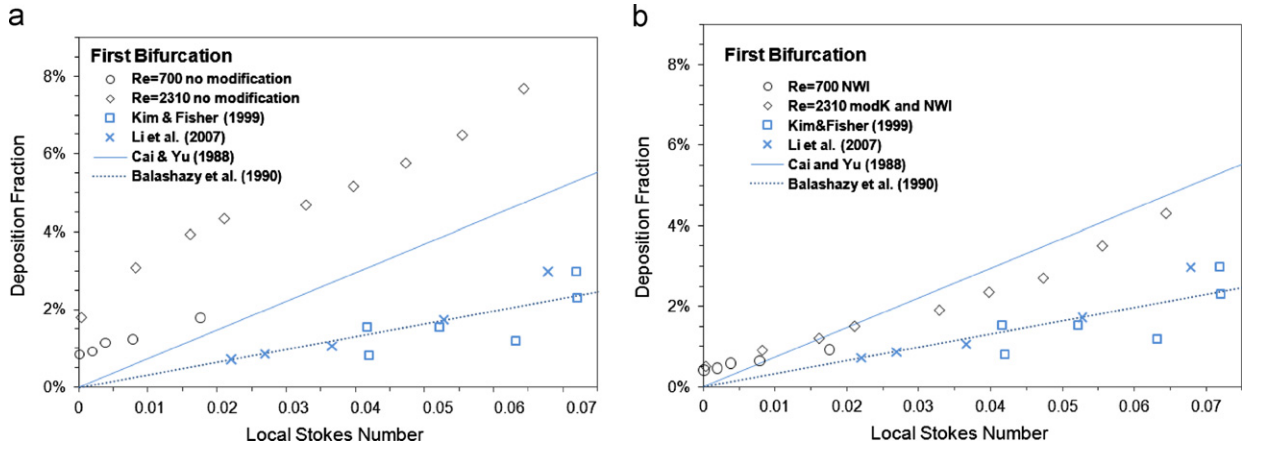

Fig. 8. Comparison of the deposition efficiency in the first generation of the CFD simulations replica with reported lung cast deposition data and theoretical models. Bifurcation 1.

Fleming, & Bailey, 2002; Weibel, 1963). In general the right side of the modelled airway was found to be larger in diameter than the left side. The recovery is measured as the percentage increase in the diameters from the Asthma Model to the Recovered Model. This may be thought of as the airway recovery in terms of a % in dilation from the asthma affected state. A large increase was expected for the branches that were severely affected by the asthma (G4LU and G4RU). Besides these affected branches, G3LL and G3RU also had a dilation greater than 10% (Figs. 9 and 10). Overall the right airway exhibited greater dilation in comparison with the left airway especially from the fifth generation onwards. The average dilation in the right airway is 10.4% while for the left airway it is 4.8%. Three generation sections, G3LU, and G6R showed minor negative increases (-0.2% and -0.4%, respectively) which means that these sections were actually contracted. Since only one model has been used in this study, it is uncertain if this is within the margin of the modelling error or whether it reflects a real physiological feature such as the after effects of airway narrowing by inflammation and edema of the lining airway mucosa, or even the accumulation of mucus and other fluids, which can plug the airways.

The bifurcation at the G1–G2 branches produces the right main bronchus at a more obtuse angle than that of the left main bronchus measured by the interbronchial axis (centreline of the bronchus) with the long axis of the trachea. The right main bronchus continues and bifurcates posterior and inferiorly into the right upper lobe bronchus (GR3U) and an intermediate bronchus (GR3L). This bifurcation occurs earlier on the right than on the left lung in all models. The sum of the two daughter branching angles (i.e. G1–G2 angle $\theta \approx 80^\circ$) form the tracheal carinal angle which compares with a mean value of 73° (Karabulut, 2005). Bifurcation angles is changed slightly after recovery from asthma. The airway recovery not only changes the airway diameter but also the orientation of the airway geometry which may prove to be more significant than dilation effects alone.

3.4. Airflow distribution and pressure coefficient

Airway resistance is caused by the viscous losses due to the friction between the air and the surrounding branch walls. This causes a pressure drop in the airflow which requires mechanical effort by the respiratory muscles to overcome. A larger pressure drop over the same distance requires greater breathing efforts. In Fig. 11 contours of the pressure coefficient in reference to the inlet boundary conditions are shown for a flow rate of 10 L/min. The pressure coefficient is defined as:

$$C_p = \frac{(p - p_{ref})}{\frac{1}{2}\rho_{ref} v_{ref}^2} \tag{14}$$

where p is the static pressure, p_{ref} is the reference pressure taken as 0 Pa, and $\frac{1}{2}\rho_{ref} v_{ref}^2$ is the reference dynamic pressure. The asthma affected model exhibits the greatest resistance; nearly two times greater than the recovered model (ΔP_{AA}=4.67 Pa; ΔP_{REC}=2.72 Pa). The required pressure difference at the inlet for the Asthma Model was nearly twice the value for the recovered model. This suggests that during the period of an acute asthma episode, the work of breathing for the patient in order to achieve the same tidal volumes is double compared to the recovered state, which can lead to respiratory muscle fatigue. Along the main bronchus the pressure decreases steadily while there is a definite pressure drop from each main branch into the subsequent daughter branch. This is due to the bifurcation ridge where a local maximum occurs as a result of a build up of pressure, similar to a stagnation point. Airflow distribution through individual branches

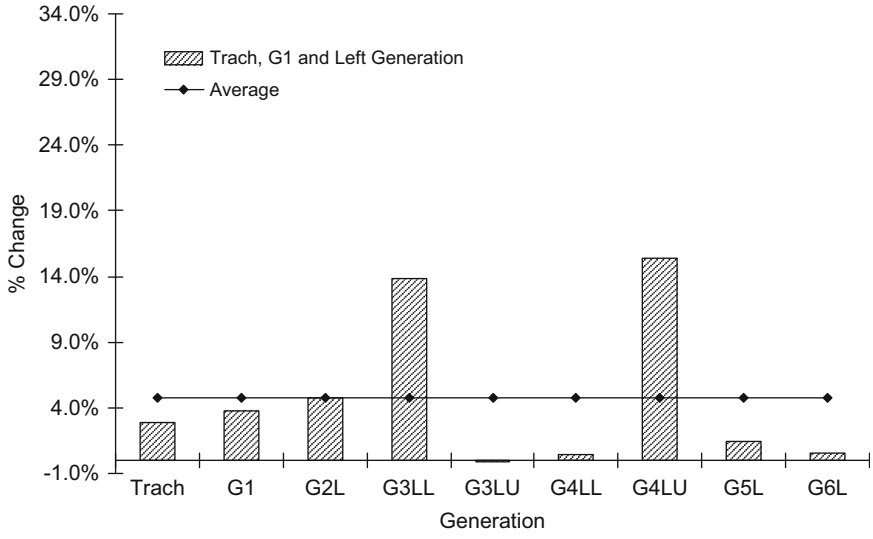

Fig. 9. Percentage increase in the averaged diameter from the acute asthma model to the recovered model in the trachea, first generation and the left airway.

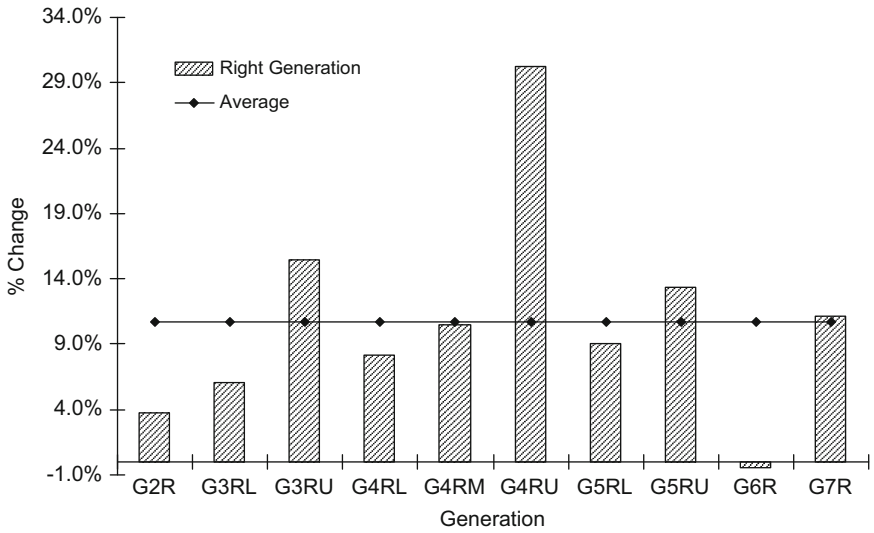

Fig. 10. Percentage increase in the averaged diameter from the acute asthma model to the recovered model in the right airway.

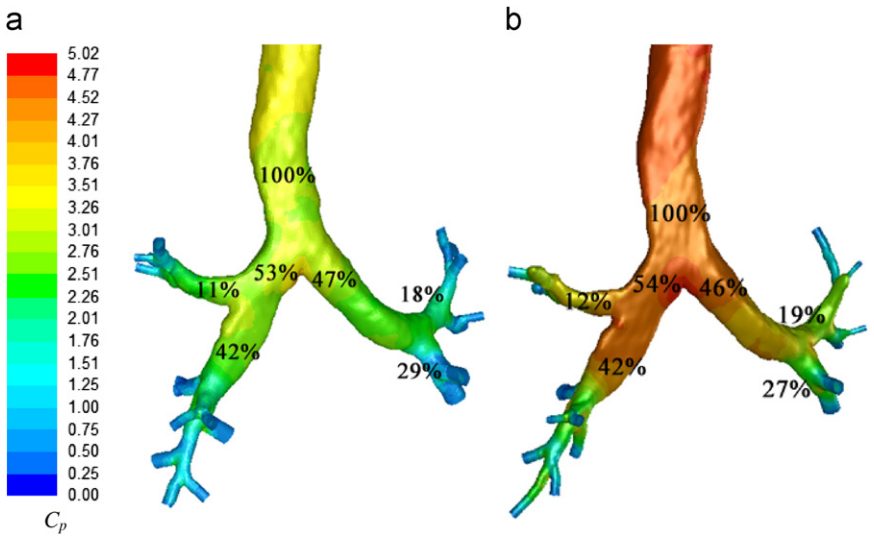

Fig. 11. Pressure coefficient, C_p values referenced against inlet boundary conditions and branch outlets set at 0 pa: (a) Recovered model, ΔP_{REC} = 2.72 Pa and (b) Asthma model, ΔP_{AA} = 4.67 Pa.

shows a similar trend among the two models. Greater mass flow rate passes through the right main bronchus (53–59%) which continues down the right intermediate bronchus (40–42%). The greater flow through the right lung is mainly attributed to the right lung being larger than the left lung. To accommodate this, the diameter of the right bronchus is therefore larger than the left one. On the left airway, the main continuation is also downwards along the left lower lobe bronchus. There is only a small proportion entering the upper lobes of both sides of the airway, which is due to the lateral curve. It is therefore apparent that the branching angle has a significant influence on the airflow distribution. Similar flow characteristics were found for the higher flow rate of 30 L/min which produced a maximum pressure coefficient of 28.87 for the Asthma Model. Since the pressure coefficient distribution was very similar the qualitative image is not shown for brevity.

3.5. *Particle deposition comparisons*

Particle deposition fractions in the first and second bifurcations are compared between the recovered model and the asthma affected model, while the deposition efficiency for the six-generation airway under the laminar and turbulent flow rate is also compared (Fig. 11). The difference in deposition between the two models in the first bifurcation is not as great as it is in the second bifurcation. For $St < 0.04$ the average deposition fraction difference is 0.35% and for St (0.04–0.07) the

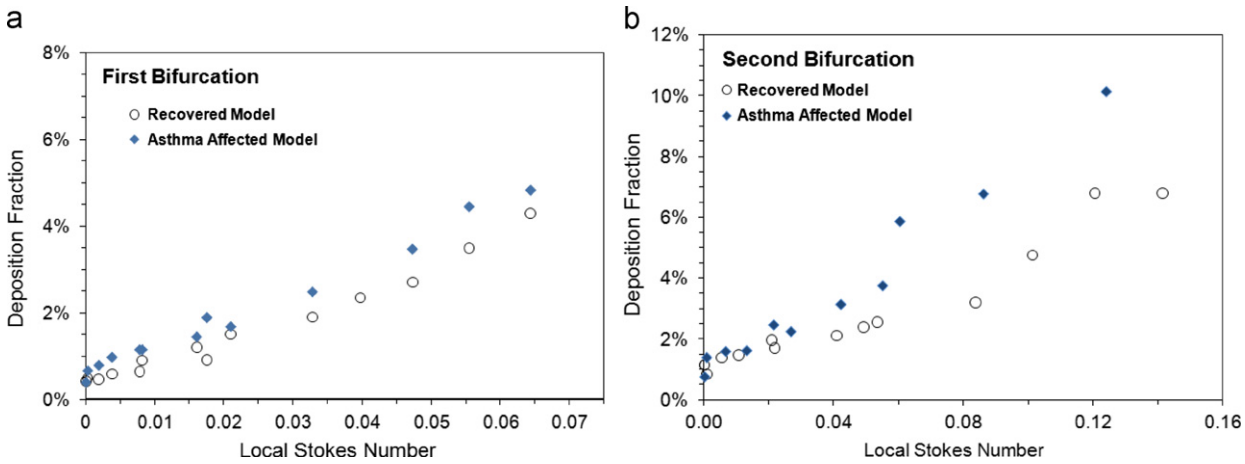

Fig. 12. Deposition fraction comparison between the recovered and Asthma Model in the (a) 1st bifurcation and (b) 2nd bifurcation.

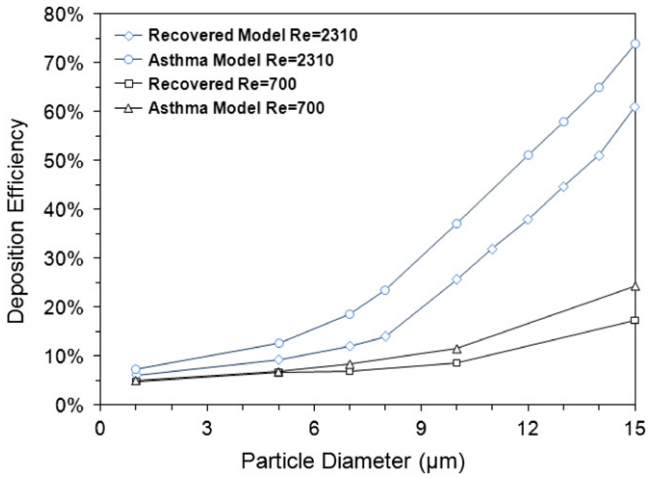

Fig. 13. Deposition efficiency comparison through the entire six-generation model for Re=700 and Re=2310.

difference is 0.73%. In the second bifurcation, the airway becomes smaller contributing to higher Stokes numbers. For $St < 0.06$ the average deposition fraction difference is 0.73% and for St (0.06–0.15) the difference is 3.1%. The larger the particle the greater the deposition fraction becomes. As the particles travel further downstream the deposition fractions between the two models is likely to exhibit similar differences. The total deposition efficiency for the six-generation airway model is the accumulation of the deposition fractions at each bifurcation region. It is found for smaller particle sizes ($< 6\,\mu m$), there is little difference in the deposition efficiency, and therefore the effects of the airway obstruction is not significant. For larger particles ($> 6\,\mu m$) the airway obstructions caused by asthma becomes significant, reaching a maximum difference of 7.1% for 15 μm particles for a laminar flow. When the flow rate is increased (three fold) and the flow becomes turbulent, the effects of the asthma on the particle deposition is enhanced even further. A maximum difference of 13% between the two models is found for particles $\geq 10\,\mu m$ (Figs 12 and 13).

3.6. 5 μm particle deposition patterns

Five μm particles were chosen for the qualitative results as this particle size is a good representation for drug particle delivery in the lower respiratory tract, given that larger particles may deposit prematurely in the oral and pharyngeal region, and smaller particles will have fewer deposition. Deposition patterns for the computational models allow visualisation which allows deeper insight into the connections between the airway geometry and deposition sites. Fig. 14 shows the concentration of particles generally impacting at each bifurcation as the airflow begins to separate. The percentage values displayed next to the outlets represent the percentage of particles that escape through those outlets. This shows that a large proportion of particles are travelling through the right main bronchus which leads to greater exposure to the particles. In addition approximately 40% of inhaled 5 μm particles penetrate past the sixth bifurcation via

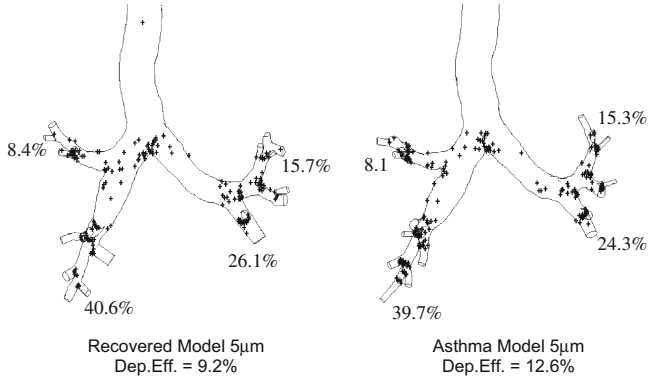

Fig. 14. Particle deposition pattern and particle outlet distribution comparison for 5 μm particles.

the right main bronchus. The lowest escaped particles are found in the upper right bronchus and the upper left bronchus, which are caused by the larger bifurcation angles as well as the G3L-dorsal angles (Table 1). Comparisons between the Recovered Model and the Asthma Model show a deposition of 9.2% and 12.6%, respectively.

4. Discussion

Ventilation in the respiratory airway is accomplished by the transport of inspired air down pressure gradients within the airways. This process involves the alternating contraction and relaxation of the respiratory muscles which overcomes the pressure drop caused by viscous losses such as shearing forces within the fluid, the friction between the air and walls of the airways, and the resistance presented by the irregularities of the airways. Under steady laminar flow conditions of 10 L/min the required effort by the respiratory muscle to overcome the pressure difference for the Asthma Model is nearly twice as high as the Recovered Model. The primary cause of greater resistance in the Asthma Model is the narrowed airways especially in the third and fourth airway generations (see Fig. 11). This suggests that during the an acute asthma episode, the effort for a patient required to breathe the same tidal volume is doubled compared to a recovered state, which can lead to respiratory muscle fatigue. The walls created within the model are assumed rigid and smooth whereas in reality the walls may exhibit some roughness and elasticity. The inclusion of these attributes would lead to greater detail in this area of study through the fluid-structure-interaction (FSI) modelling approach. The FSI model will indeed alter the predicted magnitudes of the pressure drop, as the modelling involves two or four way coupling, however it is uncertain if the comparative ratio between the two pressure drops will change much. Furthermore the inclusion of the airway material data is difficult to define since approximations the elasticity and roughness of the airway walls is not well known.

Treatment of asthma is most commonly employed during the onset of the asthma episode. Particles are atomised into smaller particles through ventilators or other drug delivery devices and inhaled through the mouth. In this study the particle deposition patterns showed that the airway geometry had an effect when the particle size was large and/or when the air flow was increased. Drug particles are delivered with the target being the region of airway occlusion; however the deposition patterns show that particles travel through regions where the geometry does not deviate greatly and eventually deposit at the bifurcation carina. The results showed that a significant number of particles pass through the right main bronchus and therefore deposition of particles will be in the right lung airways. This is a consequence of the airway branching angle at the carina bifurcation which produces the left main bronchus at a more obtuse angle than that of the right main bronchus. This feature also affects small Stokes numbered particles, where approximately 40% of the particles, introduced at the trachea inlet penetrate past the sixth generation in the right lung airways. Therefore the efficacy of drug delivery will be low if the occluded airway is deep in the left lung airways and lead to acute overdose in the localised regions of the right lung airways unnecessarily. Studies published by Kim et al. (1983), Kim et al. (1989), and Kim (1989) corroborate the simulation findings where the aerosol deposition increased greatly in patients with obstructive airway disease without regard to type of obstructions.

In terms of targeted drug delivery studies in the lung airways, the deposition patterns will be under-predicted for airway models that are reconstructed from a healthy or non-asthma affected lung airway. The discrepancy may reach as high as 13% between the two models for particles $\geq 10\,\mu m$ under a turbulent flow. From a practical viewpoint, this discrepancy may not be critical since drug particles intended for the pulmonary regions need to be smaller than 10 μm, to navigate through the upper airways (mouth, larynx, pharynx). For particles $< 10\,\mu m$, the discrepancy reduces to 3.4% for 5 μm and 1% for 1 μm under a turbulent flow. This is more significant for drug delivery since smaller size particles (1–3 μm diameter) are more likely to reach the lung airways for deep lung deposition. The average airway branch difference from the Asthma Model to the Recovered Model was found to be 10.4% in the right airway and 4.8% in the left airway; however the airway dilation during the recovery stage was not a consistent through the entire branch airway. Instead there were local branches that exhibited very high dilation recovery (GR4U $\approx$ 30% recovery) and some may have even exhibited

contraction (G3LU $\approx -0.2\%$). This dilation recovery makes it quite difficult to predict where and how much each branch will recover from an asthma episode.

5. Conclusion

Two models with six generations of the airway tree from an acute asthma episode and following recovery from the same patient 30 days apart were reconstructed from computed tomography (CT) scans in order to investigate the effects of acute asthma on a realistic airway geometry, the airflow patterns, the pressure drop, and the implications it has on targeted drug delivery. The comparisons in the geometry found that in general the right side of the airway is larger in diameter than the left side. The recovery of the airway was most significant in the severely asthma affected regions. Overall the right airway exhibited greater dilation in comparison with the left airway especially from the fifth generation onwards. The required pressure difference at the inlet for the Asthma Model was nearly twice the value for the recovered model. This suggests that during the period of an acute asthma episode, the work of breathing for the patient in order to achieve the same tidal volumes is double compared to the recovered state, which can lead to respiratory muscle fatigue. Particle deposition patterns showed that the changes in the airway had significant influence on flow patterns. A majority of the particles deposited passed through or deposited in the right lung airways, as a consequence of the biased carina bifurcation. It was also shown that the narrowing of the airway magnifies the effects of the airway curvatures. This means that studies of drug delivery in the lung airway should consider the effects of airway narrowing and that if a recovered or a healthy airway is used, then the deposition fraction and efficiencies are expected to be under-predicted.

Acknowledgements

The financial support provided by the Australian Research Council (project ID LP0989452) and by RMIT University through an Emerging Research Grant are gratefully acknowledged. The third author (Mr Ye) would also like to thank the Australian Government and RMIT University for providing him with a Scholarship through Australian Postgraduate Award (APA).

References

Balashazy, I., & Hofmann, W. (1993). Particle deposition in airway bifurcations – I. Inspiratory flow. *Journal of Aerosol Science*, *24*, 745–772.
Balásházy, I., Hofmann, W., & Martonen, T. B. (1990). Inertial impaction and gravitational deposition of aerosols in curved tube and airway bifurcations. *Aerosol Science and Technology*, *13*(3), 308–321.
Cai, F. S., & Yu, C. P. (1988). Inertial and interceptional deposition of spherical particles and fibres in a bifurcating airway. *Journal of Aerosol Science*, *19*(6), 679–688.
Calay, R. K., Kurujareon, J., & Holdo, A. E. (2002). Numerical simulation of respiratory flow patterns within human lung. *Respiratory Physiology and Neurobiology*, *130*, 201–221.
Cash, J. R., & Karp, A. H. (1990). A variable order Runge–Kutta method for initial value problems with rapidly varying right-hand sides. *ACM Transactions on Mathematical Software*, *16*, 201–222.
Chalupa, D. C., Morrow, P. E., Oberdorster, G., Utell, M. J., & Frampton, M. W. (2004). Ultrafine particle deposition in subjects with asthma. *Environmental Health Perspectives*, *112*(8), 879–882.
Chang, H. K., & El Masry, O. A. (1982). A model study of flow dynamics in human central airways. *Respiratory Physiology*, *49*(1), 75–95.
Choi, L. T., Tu, J. Y., Li, H. F., & Thien, F. (2007). Flow and particle deposition patterns in a realistic human double bifurcation airway model. *Inhalation Toxicology*, *19*, 117–131.
Clark, A. R. (1995). Medical aerosol inhaler: Past, present and future. *Aerosol Science and Technology*, *22*(4), 374–391.
De Backer, J. W., Vos, W. G., Devolder, A., Verhulst, S. L., Germonpré, P. Wuyts, F. L., et al. (2008). Computational fluid dynamics can detect changes in airway resistance in asthmatics after acute bronchodilation. *Journal of Biomechanics*, *41*(1), 106–113.
de Rochefort, L., Vial, L., Fodil, R., Maitre, X., Louis, B. Isabey, D., et al. (2007). In vitro validation of computational fluid dynamic simulation in human proximal airways with hyperpolarized 3He magnetic resonance phase-contrast velocimetry. *Journal of Applied Physiology*, *102*(5), 2012–2023.
Farkas, A., & Balásházy, I. (2007). Simulation of the effect of local obstructions and blockage on airflow and aerosol deposition in central human airways. *Aerosol Science*, *38*, 865–884.
Graham, D. I., & James, P. W. (1996). Turbulent dispersion of particles using eddy interaction models. *International Journal of Multiphase Flow*, *22*(1), 157–175.
Hofmann, W., Golser, R., & Balashazy, I. (2003). Inspiratory deposition efficiency of ultrafine particles in a human airway bifurcation model. *Aerosol Science and Technology*, *37*(12), 988–994.
Isabey, D., & Chang, H. K. (1981). Steady and unsteady pressure-flow relationships in central airways. *Journal of Applied Physiology*, *51*, 1338–1348.
Kallio, G. A., & Reeks, M. W. (1989). A numerical simulation of particle deposition in turbulent boundary layers. *International Journal of Multiphase Flow*, *15*(3), 433–446.
Karabulut, N. (2005). CT assessment of tracheal carinal angle and its determinants. *British Journal of Radiology*, *78*, 787–790.
Kim, C. S., Brown, L. K., Lewars, G. G., & Sackner, M. A. (1983). Deposition of aerosol particles and flow resistance in mathematical and experimental airway models. *Journal of Applied Physiology*, *55*(1), 154–163.
Kim, C. S., Eldridge, M. A., Garcia, L., & Wanner, A. (1989). Aerosol deposition in the lung with asymmetric airways obstruction: In vivo observation. *Journal of Applied Physiology*, *67*(6), 2579–2585.
Kim, C. S. (1989). Aerosol deposition in the lung with obstructed airways. *Journal of Aerosol Medicine*, *2*(2), 111–120.
Kim, C. S., & Fisher, D. M. (1999). Deposition characteristics of aerosol particles in sequentially bifurcating airway models. *Aerosol Science and Technology*, *31*, 198–220.
Kim, C. S., & Kang, T. C. (1997a). Comparative measurement of lung deposition of inhaled fine particles in normal subjects and patients with obstructive airway disease. *American Journal of Respiratory and Critical Care Medicine*, *155*, 899–905.
Kim, C. S., & Kang, T. C. (1997b). Comparative measurement of lung deposition of inhaled fine particles in normal subjects and patients with obstructive airway disease. *American Journal of Respiratory and Critical Care Medicine*, *155*(3), 899–905.

Li, Z., Kleinstreuer, C., & Zhang, Z. (2007a). Particle deposition in the human tracheobronchial airways due to transient inspiratory flow patterns. *Aerosol Science*, *38*, 625–644.
Li, Z., Kleinstreuer, C., & Zhang, Z. (2007b). Simulation of airflow fields and microparticle deposition in realistic human lung airway models. Part I: Airflow patterns. *European Journal of Mechanics B/Fluids*, *26*, 632–649.
Longest, P. W., & Vinchurkar, S. (2009). Inertial deposition of aerosols in bifurcating models during steady expiratory flow. *Journal of Aerosol Science*, *40*(4), 370–378.
Longest, P. W., Vinchurkara, S., & Martonen, T. (2006). Transport and deposition of respiratory aerosols in models of childhood asthma. *Aerosol Science*, *37*, 1234–1257.
Luo, H. Y., & Liu, Y. (2009). Particle deposition in a CT-scanned human lung airway. *Journal of Biomechanics*, *42*(12), 1869–1876.
Martonen, T., Fleming, J., Schroeter, J., Conway, J., & Hwang, D. (2003). In silico modeling of asthma. *Advanced Drug Delivery Reviews*, *55*, 829–849.
Matida, E. A., Finlay, W. H., Lange, C. F., & Grgic, B. (2004). Improved numerical simulation for aerosol deposition in an idealized mouth-throat. *Journal of Aerosol Science*, *35*, 1–19.
Menon, A. S., Weber, M. E., & Chang, H. K. (1984). Model study of flow dynamics in human central airways. Part III: Oscillatory velocity profiles. *Respiration Physiology*, *55*, 255–275.
Morsi, S. A., & Alexander, A. J. (1972). An investigation of particle trajectories in two-phase flow systems. *Journal of Fluid Mechanics*, *55*(2), 193–208.
Musante, C. J., & Martonen, T. B. (2001). Computational fluid dynamics in human lungs II. Effects of airway disease. In T. B. Martonen (Ed.), *Medical applications of computer modelling: The respiratory system*. Boston, MA: Wit Press.
Pedley, T. J., Schroter, R. C., & Sudlow, M. F. (1977). Gas flow and mixing in the airways. In J. West (Ed.), *Bioengineering aspects of the lung*. New York: Dekker.
Roland, N. J., Bhalla, R. K., & Earis, J. (2004). The local side effects of inhaled corticosteroids: Current understanding and review of the literature. *Chest*, *126*(213), 213–219.
Sauret, V., Halson, P. M., Brown, I. W., Fleming, J. S., & Bailey, A. G. (2002). Study of the three-dimensional geometry of the central conducting airways in man using computed tomographic (CT) images. *Journal of Anatomy*, *200*, 123–134.
Sbirlea-Apiou, G., Lemaire, M., Katz, I., Conway, J., Fleming, J. S., & Martonen, T. B. (2004). Simulation of the regional manifestation of asthma. *Journal of Pharmaceutical Sciences*, *93*(5), 1205–1216.
Schlesinger, R. B., Gurman, J. L., & Lippmann, M. (1982). Particle deposition within bronchial airways: Comparisons using constant and cyclic inspiratory flows. *Annals of Occupational Hygiene*, *26*(1), 47–64.
Schroter, R. C., & Sudlow, M. F. (1969). Flow patterns in models of the human bronchial airways. *Respiration Physiology*, *7*, 341–355.
Slutsky, A. S., Berdine, G. G., & Drazen, J. M. (1981). Oscillatory flow and quasi-steady behavior in a model of human central airways. *Journal of Applied Physiology*, *50*(6), 1293–1299.
Sullivan, K. J., & Chang, H. K. (1991). Steady and oscillatory trans-nasal pressure-flow relationships in healthy adults. *Journal of Applied Physiology*, *71*, 983–992.
van Ertbruggen, C., Hirsch, C., & Paiva, M. (2005). Anatomically based three-dimensional model of airways to simulate flow and particle transport using computational fluid dynamics. *Journal of Applied Physiology*, *98*, 970–980.
Wang, Y., & James, P. W. (1999). On the effect of anisotropy on the turbulent dispersion and deposition of small particles. *International Journal of Multiphase Flows*, *25*, 551–558.
Weibel, E. R. (1963). *Morphometry of the human lung*. New York, US: Academic Press.
Yang, X. L., Liu, Y., & Luo, H. Y. (2006). Respiratory flow in obstructed airways. *Journal of Biomechanics*, *39*, 2743–2751.
Zhang, Z., & Kleinstreuer, C. (2001). Effect of particle inlet distributions on deposition in a triple bifurcation lung airway model. *Journal of Aerosol Medicine – Deposition Clearance and Effects in the Lung*, *14*, 13–29.
Zhang, Z., Kleinstreuer, C., & Kim, C. S. (2001). Flow structure and particle transport in a triple bifurcation airway model. *Journal of Fluids Engineering – Transactions of the ASME*, *123*, 320–330.
Zhang, Y., Finlay, W. H., & Matida, E. A. (2004). Particle deposition measurements and numerical simulation in a highly idealized mouth-throat. *Journal of Aerosol Science*, *35*(7), 789–803.
Zhang, Z., Kleinstreuer, C., Kim, C. S., & Hickey, A. J. (2002). Aerosol transport and deposition in a triple bifurcation bronchial airway model with local tumours. *Inhalation Toxicology*, *14*, 1111–1133.
Zhou, Y., & Cheng, Y. S. (2005). Particle deposition in a cast of human tracheobronchial airways. *Aerosol Science and Technology*, *39*, 492–500.